

Generation of photon energy deposition kernels using the EGS Monte Carlo code

This content has been downloaded from IOPscience. Please scroll down to see the full text.

1988 Phys. Med. Biol. 33 1

(<http://iopscience.iop.org/0031-9155/33/1/001>)

View [the table of contents for this issue](#), or go to the [journal homepage](#) for more

Download details:

IP Address: 149.142.243.72

This content was downloaded on 17/02/2017 at 16:23

Please note that [terms and conditions apply](#).

You may also be interested in:

[Beam hardening of 10 MV radiotherapy X-rays: analysis using a convolution/superposition method](#)

P E Metcalfe, P W Hoban, D C Murray et al.

[Dose calculations for external photon beams in radiotherapy](#)

Anders Ahnesjö and Maria Mania Aspradakis

[Photon beam convolution using polyenergetic energy deposition kernels](#)

P W Hoban, D C Murray and W H Round

[A cobalt-60 primary dose spread array derived from measurements](#)

J E O'Connor and D E Malone

[Monte Carlo techniques in medical radiation physics](#)

P Andreo

[Stopping power data for high-energy photon beams](#)



P Andreo and A Brahme

[Point kernels and superposition methods for scatter dose calculations in brachytherapy](#)


Åsa K Carlsson and Anders Ahnesjö

[X-ray dose computations in heterogeneous media using 3-dimensional FFT convolution](#)


Y Zhu and A Boyer



**Implementing MRI & MR-SIM
for Radiation Oncology: What You
Need to Know by Dr. Glide-Hurst**



Register
Now!



modusQA
Accuracy. Confidence.™

Generation of photon energy deposition kernels using the EGS Monte Carlo code

T R Mackie^{†||}, A F Bielajew[‡], D W O Rogers[‡] and J J Battista[§]

[†] Physics Services, Allan Blair Memorial Clinic, Regina, Canada, S4T 7T1

[‡] Physics Division, National Research Council of Canada, Ottawa, Canada, K1A 0R6

[§] Department of Medical Physics, Cross Cancer Institute, Edmonton, Canada, T6G 1Z2

Received 8 September 1986, in final form 29 April 1987

Abstract. The EGS Monte Carlo code was used to generate photon energy deposition kernels which describe the energy deposited by charged particles set in motion by primary, first scattered, second scattered, multiple scattered and bremsstrahlung plus annihilation photons. These were calculated for a water medium irradiated with monoenergetic photons with energies in the range 0.1–50 MeV. In addition to the primary energy deposition kernels, primary charged particle transport was further characterised by computing the effective centre of the voxels, and the effective penetration depth, effective radius and effective lateral distance travelled by these particles. The dose per unit collision kerma for parallel monoenergetic primary photons β' was calculated. Additional applications of the energy deposition kernels are discussed.

1. Introduction

A number of authors have proposed that photon dose be calculated using convolution mathematics (Dean 1980, Mackie 1983, 1984, Mackie and Scrimger 1984, Boyer and Mok 1984, 1985, Ahnesjo 1984, Boyer 1984, Chui *et al* 1984, Mackie *et al* 1985b, Mohan *et al* 1986). The technique involves convolving the primary photon fluence with a kernel that describes the transport and deposition of energy by secondary particles. The convolution kernel has been termed a dose spread array because it describes the spread of dose from a primary photon interaction site (Mackie *et al* 1985b). Mohan *et al* (1986) have called the convolution kernel a 'differential pencil beam'.

In principle, the energy deposition kernels can be obtained by deconvolving measured narrow beam dose distributions (Ahnesjo 1984). Alternatively, one can calculate monoenergetic energy deposition kernels using Monte Carlo simulation. In this approach, the contributions from each photon scattering order (e.g. primary, first scatter, etc) may be obtained separately (Mackie *et al* 1985b). The transport of several orders of photon scattering may be modelled analytically, but higher-order scattering is more effectively modelled with the Monte Carlo method.

Roesch (1958) defined a distribution called an 'influence function' which is equivalent to a primary energy deposition kernel and showed how it could be used to obtain the amount of dose deposited in situations of electronic disequilibrium. The influence function was not calculated but its first moments, called \bar{x} in the incident photon direction and \bar{y} in the perpendicular direction, were estimated. The first moment \bar{x} was used to approximate the ratio of dose to collision kerma β (Loevinger 1981). Brahme (1977) analytically estimated a distribution equivalent to the primary energy deposition kernel and the influence function.

^{||} Currently at: Department of Medical Physics, 1300 University Avenue, University of Wisconsin, Madison, WI 53706, USA.

The EGS (electron gamma shower) Monte Carlo code is a general purpose photon-charged-particle transport simulation system which can be used for medical physics problems (Ford and Nelson 1978, Rogers 1982, 1984, Mackie *et al* 1985a, Rogers and Bielajew 1985, Mohan and Chui 1985, Mohan *et al* 1986). It was originally written at Stanford Linear Accelerator Center (SLAC) to describe the transport through matter of photons and charged particles (electrons and positrons) from very high-energy linear accelerators and cosmic rays. It has recently been modified (Rogers 1984, Nelson *et al* 1985) for improved simulation of the transport of particles with energies relevant to those encountered in medical physics.

This paper reports the use of EGS to produce energy deposition kernels in water for several scattering orders at a wide range of incident photon energies. Although the original motivation for this work was to produce a data base for the convolution method of calculating dose distributions in radiotherapy, we have also computed fundamental information that can be of use to predict the energy deposition behaviour of secondary particles following photon interactions.

2. Generation of energy deposition kernels

2.1. Geometry of the simulated phantom

An EGS user code called SCASPH (scatter spherical) modelled the passage of photons and charged particles in a homogeneous sphere of water with a radius of 60 g cm^{-2} . Incident photons were forced to interact at the centre of the sphere and secondary particles generated. The history of any particle which escaped the phantom was terminated.

There was rotational symmetry about an axis defined by the incident photon direction. The polar angle with respect to this axis and the radius from the origin completely specified the voxel boundaries. Figure 1 illustrates a volume element (voxel) defined in spherical coordinates. The voxel boundaries were defined at the intersection of 48 cones (each separated by a polar angle of 3.75°) and 24 radial shells. The distance between the shells was smaller nearer the origin. The smallest radial spacing was

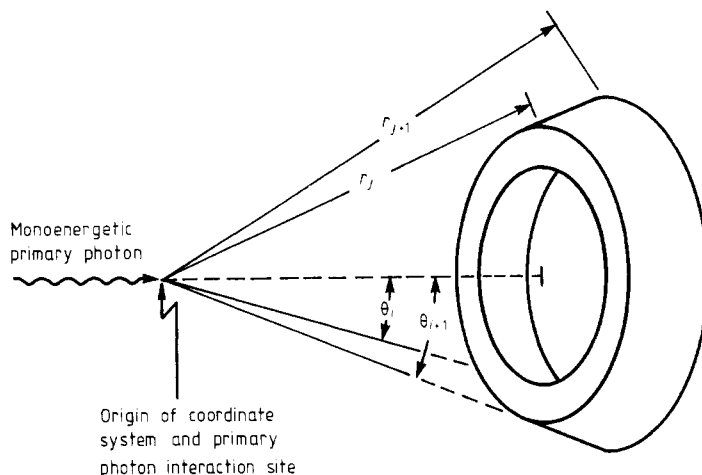


Figure 1. Illustration of a volume element (voxel) in a spherical water phantom with a radius of 60 g cm^{-2} . Monoenergetic primary photons interact at the centre of the sphere.

0.05 g cm^{-2} which occurs immediately surrounding the origin and the largest was 10 g cm^{-2} occurring near the edge of the phantom. This spatial arrangement was chosen, in part, because energy deposition is highest near the site of the incident photon and an efficient use of resources dictates that every voxel receive roughly an equal amount of energy. More importantly, finer resolution is required near the origin because the dose gradient is larger there.

2.2. The scoring of energy

The program accumulates the energy deposited in each voxel for the following scoring categories: primary, which is the energy deposited by electrons and positrons set in motion by incident photon interactions at the centre of the sphere; first scatter, which is the energy deposited by charged particles set in motion by first scattered Compton photons; and similarly for second scatter and multiple scatter components.

The energy deposition kernels for the above scattering orders exclude the contribution from bremsstrahlung and annihilation photons. A separate category was scored to account for the energy deposited from these photons created from charged particles of any of the scattering orders. Having a separate category for bremsstrahlung and annihilation photons made it possible to have a primary energy deposition kernel of finite extent. This enabled a better estimation of the effective longitudinal and lateral distance travelled by charged particles set in motion from primary photons. The scoring categories are summarised in the energy flow chart of figure 2.

In addition to forcing the incident photons to interact at the origin, first and second scatter photons were 'forced' to interact within the sphere. This 'forcing' reduces the statistical uncertainty in the results of these scattering orders. It was accomplished by finding the distance to the edge of the phantom in the direction of the photon. The actual path travelled was sampled to be less than or equal to this distance (Rogers and Bielajew 1985). This biasing was reconciled by weighting the scoring of the photon and all of its secondary particles by a fraction equal to the photon's probability of interacting in the phantom.

The program SCASPH generates energy deposition kernels for each component in terms of the energy deposited in each voxel normalised to the total energy of the incident primary photons which interact at the origin. The fractional amount of energy deposited in a voxel was determined by summing the energy deposited in all charged particle transport steps that occur in the voxel:

$$\varepsilon_c(i, j) = \sum_n [\Delta E_c(i, j)]_n (N_0 h\nu_0)^{-1} \quad (1)$$

where $[\Delta E_c(i, j)]_n$ is the amount of energy deposited in the n th charged particle step within voxel i, j and attributed to category c , N_0 is the number of incident primary photons and $h\nu_0$ is the primary photon energy. The dose per primary photon from each component c may be obtained for any voxel by dividing $\varepsilon_c(i, j)$ by the voxel mass $M(i, j)$ and multiplying by the primary photon energy $h\nu_0$:

$$D_c(i, j) = \frac{\varepsilon_c(i, j) h\nu_0}{M(i, j)}. \quad (2)$$

2.3. Calculation of the effective centre of the voxels

Since the extent of the primary energy deposition kernel is finite, there are voxels near the end of the range of the charged particles through which the particles penetrate

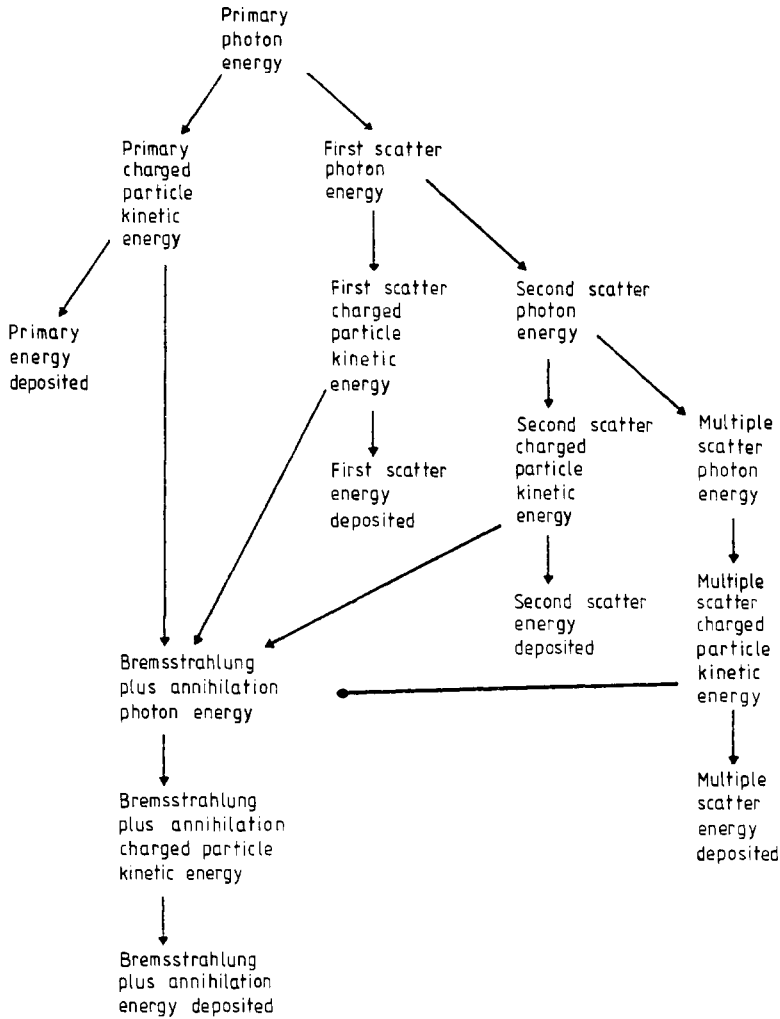


Figure 2. The partitioning of energy into the scoring categories.

only part way. Therefore, the effective centre for these voxels is uncertain. SCASPH was used to monitor the primary energy deposited within voxels and to calculate a weighted average position of the voxels. Two additional categories were scored for each voxel: the effective radius $\hat{r}_p(i, j)$ and the effective cosine, $\cos[\hat{\theta}_p(i, j)]$,

$$\hat{r}_p(i, j) = \sum_n r_n [\Delta E_p(i, j)]_n \left(\sum_n [\Delta E_p(i, j)]_n \right)^{-1} \quad (3)$$

$$\cos[\hat{\theta}_p(i, j)] = \sum_n \cos(\theta_n) [\Delta E_p(i, j)]_n \left(\sum_n [\Delta E_p(i, j)]_n \right)^{-1} \quad (4)$$

where r_n is the radius corresponding to the middle of step n , $\cos(\theta_n)$ is the cosine of the polar angle at the middle of the step and $[\Delta E_p(i, j)]_n$ is the amount of primary generated energy deposited in the n th step within voxel i, j .

These primary energy-weighted mean quantities represent the effective centre of the voxels for the primary energy deposition kernel. Multiplied together these quantities

approximate $\hat{z}_p(i, j)$, the effective depth of the voxel from the interaction site of the incident photon:

$$\hat{z}_p(i, j) \approx \hat{r}_p(i, j) \cos[\hat{\theta}_p(i, j)]. \quad (5)$$

This approximation is valid for this work because the voxel boundaries are separated by small angular increments.

2.4. EGS calculation parameters

The major EGS transport parameters used in the simulations are shown in table 1.

Charged particle transport simulations with EGS are known to be highly sensitive to the maximum fractional energy loss per step, ESTEPE (Bielajew *et al* 1985). A value of ESTEPE = 0.02 was used for the primary kernels. The details of charged particle transport were less critical for other categories because, in general, energy was being deposited in larger voxel volumes than for the primary kernels. A value of ESTEPE = 0.20 was used to speed up the calculation of these non-primary categories.

Table 1. The EGS transport parameters used in the simulations.

Name	Description of parameter†	Value of parameter
EI	Incident photon energy	0.1–50 MeV‡
NCASE	Number of incident photon histories per simulation	At least 10 ⁶
ESTEPE	Maximum fraction of electron kinetic energy lost per step via continuous energy loss	0.02 for primary energy deposition kernels, 0.2 for all other categories
ECUT'	Electron kinetic energy cut-off	4% of incident energy for incident photon energies less than 1.25 MeV, 50 keV for incident energies of 1.25 MeV or more
AE'	Secondary electron production kinetic energy threshold	
PCUT	Photon energy cut-off	
AP	Secondary photon production energy threshold	
ESAVE	Kinetic energy at which an electron history is terminated if it does not have a sufficient range to reach the boundary of a voxel	4% of incident energy for incident photon energies less than 1.25 MeV, 2.5% of incident energy for energies of 1.25 MeV or more

† The use of 'electron' in this table refers to positrons as well as electrons.

‡ See table 2 for a complete list of incident energies.

A charged particle history was terminated if its energy fell below ESAVE and there was not sufficient range for the particle to reach the voxel boundary. If this occurred, the residual kinetic energy was deposited in the voxel. This ignores the possibility of the charged particle emitting bremsstrahlung during its residual range but results in less than 1% error at 50 MeV in the category that scores bremsstrahlung energy.

Uncertainty limits (one standard deviation) were determined for each calculated quantity by dividing the calculations into 10 batches and computing the mean and root mean square deviation from the mean from these 10 values. The values of the energy deposition kernels were normalised to the number of histories so that, except for statistical fluctuations, they are independent of the number of histories.

Typical computing times for simulations using a VAX-11/780 processor (Digital Equipment Corporation) with a floating-point accelerator ranged from about 30 000 histories per CPU hour at 0.1 MeV to 1600 at 50 MeV. The total computing time to produce the kernels was the equivalent of 0.51 VAX-11/780 CPU years!

3. Results and discussion

3.1. Fraction of energy deposited

It is possible to add the energy deposited in all categories in all voxels to obtain the total amount of energy deposited within the phantom. The total energy fraction, F_{tot} , is defined to be the total energy deposited in the phantom relative to the total amount of incident photon energy interacting at the origin:

$$F_{\text{tot}} = \sum_c \sum_i \sum_j \varepsilon_c(i, j) \quad (6)$$

where $\varepsilon_c(i, j)$ is from equation (1)

The second column of table 2 lists the total energy fraction. The difference from unity represents the relative amount of energy which escapes the phantom. At a radius of 60 g cm^{-2} the phantom is large enough so that even at the highest energies over 90% of the incident photon energy is accounted for. At incident photon energies less than 300 keV over 99% of the incident energy is deposited somewhere in the phantom.

The fourth column of table 2 lists the primary energy fraction, F_p , which is the sum over all the voxels of the energy deposited from charged particles set in motion from primary photons relative to the total amount of incident primary photon energy interacting at the origin:

$$F_p = \sum_i \sum_j \varepsilon_p(i, j) \quad (7)$$

where $\varepsilon_p(i, j)$ is calculated in equation (1) for the primary component.

The primary energy fraction increases with increasing incident photon energy to 30 MeV. This is because Compton recoil electrons receive a greater fraction of the photon's energy for higher energy photons. The slight decrease after 30 MeV is because of increased bremsstrahlung which offsets the increasingly important role of pair production.

An important energy conservation check can be made since the bremsstrahlung and annihilation energy have been assigned to a separate category, and the phantom is large enough to bring to rest all of the charged particles set in motion by primary photons. The primary energy fraction F_p should be equal to the ratio of the energy absorption coefficient, μ_{en} , to the total attenuation coefficient, μ (excluding coherent scattering because we have not included it in the Monte Carlo photon transport). The ratio μ_{en}/μ is shown in the fifth column. The agreement between the values in columns 4 and 5 is within the calculated statistical uncertainty for energies below 10 MeV. Above this energy our results become smaller than the previously tabulated values which probably reflects our more accurate treatment of positron annihilation in flight (Nelson *et al* 1985).

The energy deposited can be further subdivided by determining the amount which is backscattered. This was done for each category by summing the contents of all voxels lying at polar angles greater than 90° (i.e. in the negative hemisphere). The total backscatter is listed in the third column of table 2 as a percentage of the total energy fraction. As expected, the relative amount of total energy backscattered

Table 2. The relative amount of energy deposited in a spherical phantom of radius 60 g cm^{-2} as a function of the incident photon energy. Column 2 is the fraction of incident energy deposited in the phantom from all components. Column 3 is the percentage of the total energy fraction that is backscattered. Column 4 is the fraction of incident energy deposited in the phantom from the primary component only. The ratio of energy absorption coefficient to the total attenuation coefficient in column 5 should equal the primary energy fraction. Column 6 is the percentage of the primary energy fraction that is backscattered. One standard deviation uncertainty is shown in brackets.

Incident energy (MeV)	Total energy fraction, F_{tot} (0.0004)	Percentage of total energy backscattered	Primary energy fraction, F_p (0.0002)	$\mu_{\text{en}}/\mu^{\text{a}}$ (0.001)	Percentage of primary energy backscattered
0.10	0.9981	37.27 (0.04)	0.1520	0.152 ^b	2.71 (0.01)
0.15	0.9953	33.43 (0.03)	0.1853	0.186 ^b	4.08 (0.01)
0.20	0.9928	30.08 (0.03)	0.2179	0.219 ^b	4.56 (0.01)
0.30	0.9890	24.92 (0.02)	0.2701	0.271 ^b	4.76 (0.01)
0.40	0.9859	21.28 (0.02)	0.3097	0.309	4.60 (0.01)
0.50	0.9832	18.53 (0.01)	0.3411	0.341	4.401 (0.009)
0.60	0.9808	16.41 (0.01)	0.3672	0.367	4.113 (0.009)
0.80	0.9764	13.34 (0.01)	0.4079	0.407	3.642 (0.007)
1.00	0.9726	11.22 (0.01)	0.4388	0.439	3.216 (0.007)
1.25	0.9686	9.352 (0.008)	0.4690	0.469 ^c	2.725 (0.006)
1.50	0.9646	8.034 (0.007)	0.4923	0.492	2.413 (0.006)
2.00	0.9578	6.320 (0.006)	0.5276	0.527	1.869 (0.005)
3.00	0.9476	4.569 (0.004)	0.5745	0.574	1.216 (0.003)
4.00	0.9405	3.687 (0.004)	0.6056	0.606	0.857 (0.002)
5.00	0.9362	3.157 (0.003)	0.6308	0.631	0.631 (0.002)
6.00	0.9333	2.806 (0.003)	0.6508	0.651	0.500 (0.002)
8.00	0.9304	2.352 (0.002)	0.6812	0.682	0.337 (0.001)
10.0	0.9296	2.055 (0.002)	0.7042	0.706	0.255 (0.001)
15.0	0.9306	1.583 (0.002)	0.7405	0.743	0.1560 (0.0009)
20.0	0.9316	1.282 (0.001)	0.7600	0.764	0.1088 (0.0007)
30.0	0.9300	0.9116 (0.0009)	0.7728	0.784 ^d	0.0672 (0.0005)
40.0	0.9249	0.6962 (0.0007)	0.7705	0.784 ^d	0.0506 (0.0005)
50.0	0.9177	0.5612 (0.0006)	0.7618	0.778 ^d	0.0408 (0.0004)

^a From Hubbell (1982) except where otherwise indicated.

^b From Hubbell (1969). Corrected to exclude coherent (Rayleigh) scattering. This affects values below 300 keV only.

^c From Hubbell (1977).

^d From Johns and Cunningham (1983).

decreases with increasing energy. Similarly, the primary backscatter is listed in column 6 of table 2 as a percentage of the fraction of primary generated energy deposited. The amount of primary energy backscattered also decreases with increasing energy at incident photon energies above 300 keV. The decrease in the total and primary backscatter at higher energies is because more Compton recoil electrons and scattered photons are projected forward.

In general, there is very little primary energy backscattered from the primary interaction site. This suggests that the primary component represents about 1–2% of the incident primary energy (product of the primary energy fraction and the fraction of primary energy backscattered) at the entrance surface of a megavoltage photon beam. This agrees with the estimate of Rogers and Bielajew (1985) for a ^{60}Co beam.

3.2. The effective voxel radius for the primary energy deposition kernels

The geometrical centre of a spherical voxel is specified by a radius midway between the radii defining the voxel's boundaries and an angle midway between the angles defining the voxel's boundaries. It was found that the effective angle of a voxel corresponded well with the angle through the geometrical centre. However, the geometrical centre did not always lie at the effective radius of a voxel. Table 3 compares the effective radii, $\hat{r}_p(i, j)$, for a 5.0 MeV incident photons at two angular segments with the radii corresponding to the geometrical centre. The agreement between the effective radii and the geometric radii is within 1% except at voxels lying more than 1.0 g cm^{-2} from the origin. The discrepancy between the effective radii and the geometric radii of voxels at large distances from the origin is because charged particles reach the end of their range and penetrate only part way through the voxel. Similar results were obtained at other energies. This means that at distances close to the origin the dose at the geometric centre of a spherical voxel can be taken as being equal to the mean dose in the voxel. For most purposes the geometric centre of a voxel can be used as the effective position of the voxel; however, the effective radii should be used to determine the range of charged particles set in motion from primary photons, as illustrated in § 3.3.

Table 3. The radii corresponding to the effective centre of the voxels (g cm^{-2}) for 5 MeV primary energy deposition kernels. The Monte Carlo calculated effective radii at two polar angular intervals are compared with the radii of the geometric centre of the voxels. There is no primary energy being deposited at distances greater than 3 cm. The percentage statistical uncertainty (one standard deviation) is shown in brackets.

Radius of the geometric centre (g cm^{-2})	Monte Carlo calculated effective radii (g cm^{-2})	
	0–3.75°	90–93.75°
0.025	0.025 25 (0.1)	0.0258 (0.7)
0.075	0.074 43 (0.02)	0.0748 (0.4)
0.125	0.124 3 (0.01)	0.1248 (0.2)
0.175	0.174 4 (0.01)	0.1748 (0.2)
0.250	0.248 1 (0.02)	0.2486 (0.2)
0.350	0.348 4 (0.01)	0.3486 (0.1)
0.450	0.448 4 (0.01)	0.4500 (0.1)
0.550	0.548 6 (0.01)	0.5474 (0.1)
0.700	0.695 5 (0.03)	0.6981 (0.1)
0.900	0.895 9 (0.02)	0.8957 (0.1)
1.250	1.227 (0.08)	1.215 (0.2)
1.750	1.713 (0.07)	1.673 (0.2)
2.500	2.136 (0.09)	2.047 (0.5)

3.3. The distribution of primary energy deposition

Roesch (1958) described the influence function by defining its moments in the longitudinal \bar{z} and lateral \bar{y} directions with respect to the incident photon direction. Roesch showed how these first moments could be estimated. The first moment in the longi-

tudinal direction \bar{z} (this quantity was designated as \bar{x} by Roesch (1958) and Loevinger (1981)) was described as the 'absorbed-dose-weighted mean distance of electron motion in the beam direction' (Loevinger 1981). In this work, \bar{z} will be called the effective depth of penetration. It has been used to describe the build-up in dose of the primary component of photon beams (Loevinger 1981) and beyond ' d_{\max} ' it is equivalent to the distance between equal values of collision kerma and primary absorbed dose (Loevinger 1981).

\bar{z} reflects both the distance travelled by charged particles in the direction of the primary photon as well as the amount of energy deposited as a function of depth. The following is used to define \bar{z} :

$$\bar{z} = \sum_i \sum_j \hat{z}_p(i, j) \varepsilon_p(i, j) F_p^{-1} \quad (8)$$

where $\hat{z}_p(i, j)$, $\varepsilon_p(i, j)$ and F_p are from equations (5), (1) and (7) respectively.

The effective radial distance travelled by charged particles generated by primary photons, \bar{r} , is determined in an analogous fashion:

$$\bar{r} = \sum_i \sum_j \hat{r}_p(i, j) \varepsilon_p(i, j) F_p^{-1}. \quad (9)$$

The effective lateral distance, \bar{y} , that the primary generated charged particles travel is determined from the effective depth \bar{z} and effective radius \bar{r} travelled:

$$\bar{y} = (\bar{r}^2 - \bar{z}^2)^{1/2}. \quad (10)$$

Table 4 lists the effective depth, radius and lateral distance travelled by charged particles generated from primary photons. These values increase rapidly as a function of incident photon energy. At higher incident photon energies the effective depth travelled is greater than the effective lateral distance; however, at low energies the effective lateral distance travelled is almost equal to the effective depth. The effective depth travelled \bar{z} , for a primary photon energy of 1.25 MeV, agrees well with the results of Rogers and Bielajew (1985).

The quantity, β , is defined to be the ratio of absorbed dose to collision kerma. It has been used (AAPM 1983, McEwan and Smyth 1984, Schulz and Loevinger 1984, NACP 1980, 1981) to correct for the difference between collision kerma and dose in the wall of an ion chamber. The dose per unit collision kerma can be calculated for a parallel beam of monoenergetic primary photons interacting inside a water phantom directly from the energy deposition kernels. It is here called β' to distinguish it from a determination of dose per unit collision kerma that includes scattered photons which have a spectrum of lower energies and are polydirectional:

$$\beta' = \sum_i \sum_j \exp[(\mu/\rho) \hat{z}_p(i, j)] \varepsilon_p(i, j) F_p^{-1} \quad (11)$$

where μ/ρ is the mass attenuation coefficient.

Since $(\mu/\rho) \hat{z}_p(i, j) \ll 1$, for therapeutic photon energies, a reasonable approximation to β' can be obtained using equation (8)

$$\beta' \approx 1 + (\mu/\rho) \bar{z}. \quad (12)$$

The above equation was also derived by Roesch (1958) and Loevinger (1981). β' can also be approximated with another simple equation (Roesch 1958):

$$\beta' \approx \exp[(\mu/\rho) \bar{z}]. \quad (13)$$

Table 5 contains the calculations of β' using equations (11)–(13) as well as the values of the mass attenuation coefficient μ/ρ which includes coherent (Rayleigh) scattering. The values of \bar{z} are from table 4.

Table 4. The effective depth of penetration \bar{z} , effective range \bar{r} and effective lateral distance travelled \bar{y} (g cm^{-2}) for energy deposition by charged particles generated by primary photons. The values in brackets are one standard deviation statistical uncertainty expressed as percentages.

Incident energy (MeV)	Effective depth, \bar{z} (g cm^{-2})	Effective range, \bar{r} (g cm^{-2})	Effective lateral distance, \bar{y} (g cm^{-2})
0.10	8.53×10^{-4} (0.2)	1.133×10^{-3} (0.2)	7.46×10^{-4} (0.5)
0.15	1.261×10^{-3} (0.2)	1.749×10^{-3} (0.2)	1.211×10^{-3} (0.3)
0.20	2.405×10^{-3} (0.1)	3.376×10^{-3} (0.1)	2.369×10^{-3} (0.2)
0.30	6.488×10^{-3} (0.09)	9.133×10^{-3} (0.08)	6.43×10^{-3} (0.1)
0.40	1.264×10^{-2} (0.08)	1.771×10^{-2} (0.08)	1.241×10^{-2} (0.1)
0.50	2.057×10^{-2} (0.08)	2.860×10^{-2} (0.07)	1.986×10^{-2} (0.1)
0.60	2.990×10^{-2} (0.09)	4.124×10^{-2} (0.08)	2.840×10^{-2} (0.1)
0.80	5.171×10^{-2} (0.08)	7.020×10^{-2} (0.08)	4.747×10^{-2} (0.2)
1.00	7.680×10^{-2} (0.08)	0.1026 (0.08)	6.81×10^{-2} (0.1)
1.25	0.1116 (0.07)	0.1464 (0.07)	9.48×10^{-2} (0.1)
1.50	0.1489 (0.06)	0.1924 (0.06)	0.1219 (0.1)
2.00	0.2290 (0.06)	0.2881 (0.06)	0.1748 (0.1)
3.00	0.3968 (0.06)	0.4803 (0.06)	0.2705 (0.1)
4.00	0.5714 (0.05)	0.6725 (0.05)	0.3546 (0.1)
5.00	0.7472 (0.06)	0.8619 (0.06)	0.4295 (0.1)
6.00	0.9215 (0.06)	1.0474 (0.06)	0.4918 (0.2)
8.00	1.2655 (0.05)	1.4070 (0.05)	0.6149 (0.2)
10.0	1.6013 (0.05)	1.7539 (0.05)	0.716 (0.2)
15.0	2.399 (0.05)	2.568 (0.05)	0.918 (0.2)
20.0	3.144 (0.05)	3.322 (0.05)	1.073 (0.2)
30.0	4.528 (0.05)	4.715 (0.05)	1.314 (0.3)
40.0	5.796 (0.05)	5.985 (0.05)	1.494 (0.3)
50.0	6.948 (0.05)	7.138 (0.05)	1.634 (0.03)

β' increases as a function of incident primary energy. The approximations to β' (equations (12) and (13)) are very close to the more accurate calculation using equation (11) at all energies. Indeed, equation (13) agrees with equation (11) to within the statistical uncertainty of equation (11).

Another way to describe the spatial distribution of energy deposition from charged particles set in motion by primary photons is to specify the region in which the primary component is the largest contribution. In figure 3, the median lines represent the boundary of the volume within which the primary component contributes at least half of the total for 5.0, 10.0, 20.0 and 50.0 MeV incident photons. The positions of these boundaries at large polar angles are similar. Their longitudinal extent increases almost linearly with incident photon energy. The increase in the lateral extent of the envelopes with energy is partly because the charged particles travel a greater distance laterally and partly because there is a smaller scattered photon component relative to the primary contribution.

3.4. Energy deposition kernels

Figures 4–6 illustrate the primary, first scatter and total energy deposition kernels for 1.25 MeV incident photons interacting in water. They are illustrated in isoline format

Table 5. The ratio of primary dose to collision kerma for water β' calculated using equation (11) and some approximations to β' using equations (12) and (13). Column 4 is the statistical uncertainty (one standard deviation) in β' .

Incident energy (MeV)	$\mu/\rho^{a,d}$ (cm ² g ⁻¹)	β' (equation (11))	$\delta\beta'$ (%)	$\beta' \approx 1 + (\mu/\rho)\bar{z}$	$\beta' = \exp((\mu/\rho)\bar{z})$
0.10	0.170 7	1.000 146	(0.0003)	1.000 146	1.000 146
0.15	0.150 4	1.000 190	(0.0004)	1.000 190	1.000 190
0.20	0.137 0	1.000 330	(0.0004)	1.000 330	1.000 330
0.30	0.118 7	1.000 771	(0.0008)	1.000 770	1.000 770
0.40	0.106 1	1.001 34	(0.001)	1.001 34	1.001 34
0.50	0.096 87	1.002 00	(0.002)	1.001 99	1.002 00
0.60	0.089 57	1.002 68	(0.003)	1.002 68	1.002 68
0.80	0.078 66	1.004 08	(0.004)	1.004 07	1.004 08
1.00	0.070 70	1.005 45	(0.006)	1.005 43	1.005 45
1.25	0.063 17 ^b	1.007 09	(0.007)	1.007 05	1.007 08
1.50	0.057 55	1.008 63	(0.009)	1.008 57	1.008 61
2.00	0.049 40	1.011 4	(0.01)	1.011 3	1.011 3
3.00	0.039 69	1.015 9	(0.02)	1.015 8	1.015 9
4.00	0.034 03	1.019 7	(0.02)	1.019 4	1.019 6
5.00	0.030 31	1.023 0	(0.02)	1.022 7	1.022 9
6.00	0.027 71	1.026 0	(0.05)	1.025 5	1.025 9
8.00	0.024 29	1.031 4	(0.06)	1.030 7	1.031 2
10.0	0.022 19	1.036 5	(0.07)	1.035 5	1.036 2
15.0	0.019 41	1.048 2	(0.09)	1.046 6	1.047 7
20.0	0.018 13	1.059 4	(0.1)	1.057 0	1.058 9
30.0	0.017 1 ^c	1.082	(0.1)	1.077	1.081
40.0	0.016 7 ^c	1.104	(0.2)	1.097	1.102
50.0	0.016 7 ^c	1.127	(0.2)	1.116	1.123

^a From Hubbell (1982) except where otherwise indicated.

^b From Hubbell (1977).

^c From Johns and Cunningham (1983).

^d The uncertainty in μ/ρ is 2% except at energies between 200 keV and 5 MeV for which it is 1%.

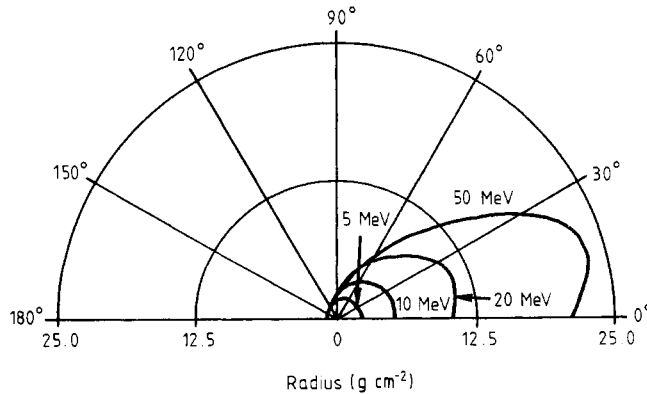


Figure 3. At each point inside the envelopes the primary component equals the sum of all other components. The envelopes increase in extent with increasing primary photon energy.

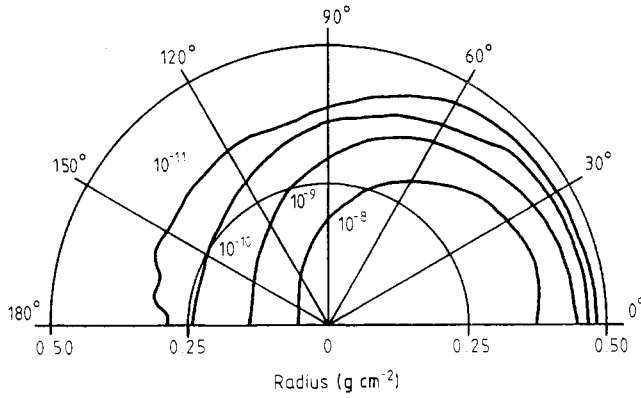


Figure 4. Primary energy deposition kernel in isoline format for 1.25 MeV photons. The units are $\text{cGy MeV}^{-1} \text{ photon}^{-1}$.

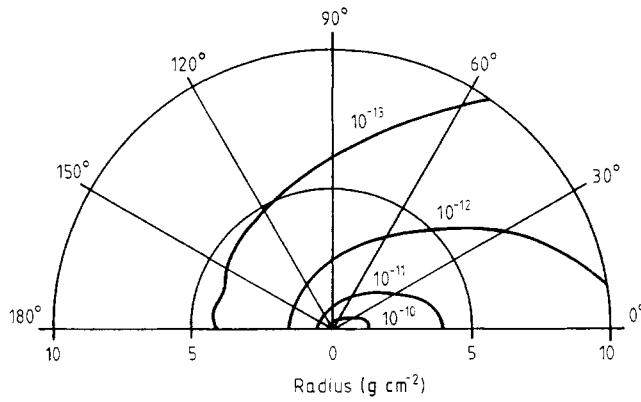


Figure 5. First scatter energy deposition kernel in isoline format for 1.25 MeV photons. The units are $\text{cGy MeV}^{-1} \text{ photon}^{-1}$.

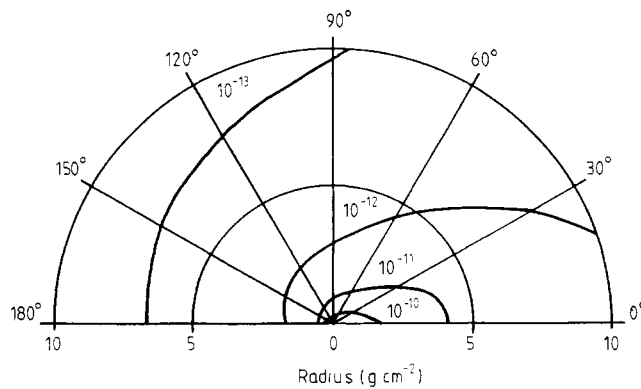


Figure 6. Total energy deposition kernel in isoline format for 1.25 MeV photons. The total energy deposition kernel is the sum of all the energy deposition kernel components. The units are $\text{cGy MeV}^{-1} \text{ photon}^{-1}$.

normalised to the total incident photon energy interacting at the origin. The units of the isolines are $\text{cGy MeV}^{-1} \text{ photon}^{-1}$. The primary kernel shown in figure 4 is contained within about 0.5 g cm^{-2} of the origin which corresponds to the position of the depth of maximum dose (d_{max}) for a ^{60}Co photon beam. Most of the energy is being deposited in the forward direction. The dose gradient near the end of the charged particle range in the direction of the incident photon is particularly steep.

The shape of the energy deposition kernel for first scatter is similar (see figure 5) to the primary kernel in that the energy is mainly deposited in the forward direction. The first scattered contribution is orders of magnitude smaller than the primary energy deposition kernel; however, the first scattered kernel contributes at distances much farther than the primary kernel.

In figure 6 all of the energy deposition kernels were summed together to obtain the total kernel. Near the primary photon interaction site, the total energy deposition kernel behaves like the primary kernel and beyond the range of the primary generated charged particles it resembles the first scattered kernel. The increased distance from the origin of the lower valued isolines is mainly because of the contribution of multiple scattered photons.

Figures 7 and 8 are examples of total energy deposition kernels at 0.1 and 10 MeV. The 0.1 MeV total kernel in figure 7 is relatively symmetric about the origin. At higher incident photon energies the kernels become more forward peaked. At 10.0 MeV (figure 8) almost no energy is being deposited in the backwards direction. At this energy, almost all of the energy is confined to a few centimetres laterally.

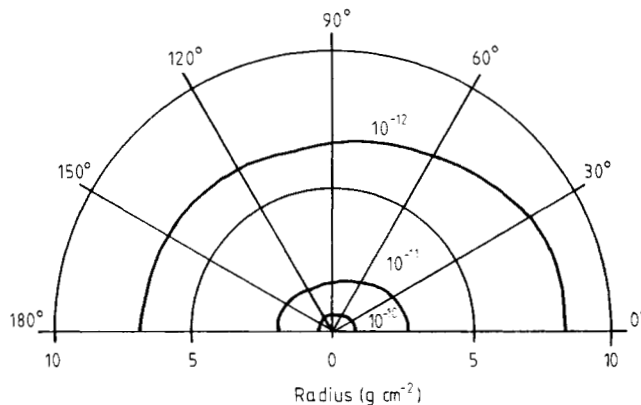


Figure 7. Total energy deposition kernel in isoline format for 0.1 MeV photons. The units are $\text{cGy MeV}^{-1} \text{ photon}^{-1}$.

There is a relatively smooth transition in the shape of the energy deposition kernels from low to high energy. This suggests that a kernel at an intermediate energy that was not calculated may be interpolated from kernels at neighbouring energies.

The total energy deposition kernels were compared with the 'differential pencil beams' of Mohan *et al* (1986). For direct comparison, the values of our total kernel were multiplied by the square of the voxel geometric radius, thereby removing the inverse square dependence. The agreement between our results and those of Mohan *et al* deviated by up to a factor of two. The differential pencil beam calculations have recently been repeated with a smaller ESTEPE value (4%) (Chui and Mohan 1986). Figures 9 and 10 are the comparisons at 5 and 20 MeV at selected angular intervals

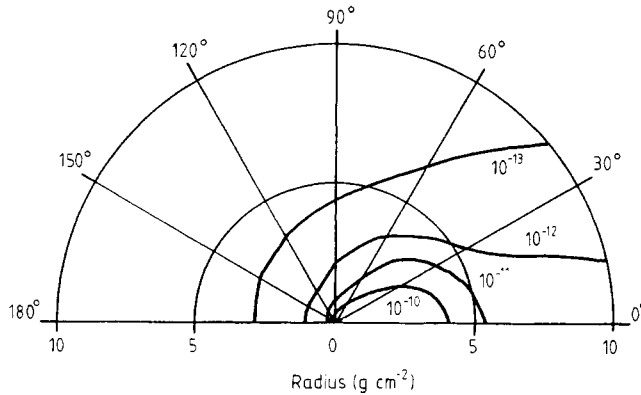


Figure 8. Total energy deposition kernel in isoline format for 10.0 MeV photons. The units are cGy MeV⁻¹ photon⁻¹.

between our results and the newer results of Chui and Mohan (1986). There is excellent agreement between the total energy deposition kernels and these differential pencil beams at large distances from the origin. The agreement at smaller distances, where the primary component dominates, is not quite as good. These small differences are unlikely to significantly affect dose distributions calculated using the convolution method. The better agreement with differential pencil beams calculated with a smaller ESTEPE reflects the crucial role of this parameter in EGS Monte Carlo simulations (Bielajew *et al* 1985).

The general shape of the curves in figures 9 and 10 is explained as follows. At angular intervals in the forward direction (between 0 and 2.56°) the total kernels close to the origin are large because most of the charged particles are initially travelling in that direction. The value decreases rapidly with radius because charged particles are scattering out of their original direction. Few charged particles are initially set in motion at larger angles (between 25.8 and 31.8° and between 45.5 and 49.5°) so the total kernel value at these angles is small. The value increases with radius as charged particles become scattered away from the forward direction. At distances close to the range of the charged particles, the total kernel value decreases with radius for all angular intervals because primary generated charged particles are being stopped. At all angular intervals the total kernels decrease more slowly with radius at distances from the origin greater than the charged particle range.

The fraction of the incident photon energy $F_c(J)$ deposited within a shell with a radius labelled J can be determined by summing the energy contained within the shell and normalising it to the total energy of the incident photons. This quantity can be expressed as:

$$F_c(J) = \sum_{j=1}^J \left(\sum_i \varepsilon_c(i, j) \right). \quad (14)$$

Figures 11–13 are graphs of the fraction of energy deposited within shells as a function of radius for the kernel categories at 500 keV, 1.25 MeV and 10 MeV. At small radii, all of the categories exhibit a power law increase in the energy deposited as a function of radius. The rate of increase for higher scattering orders is greater than for lower orders. Since the charged particles set in motion from primary photons have a finite range, the primary category reaches a plateau value at a radius equal to the maximum

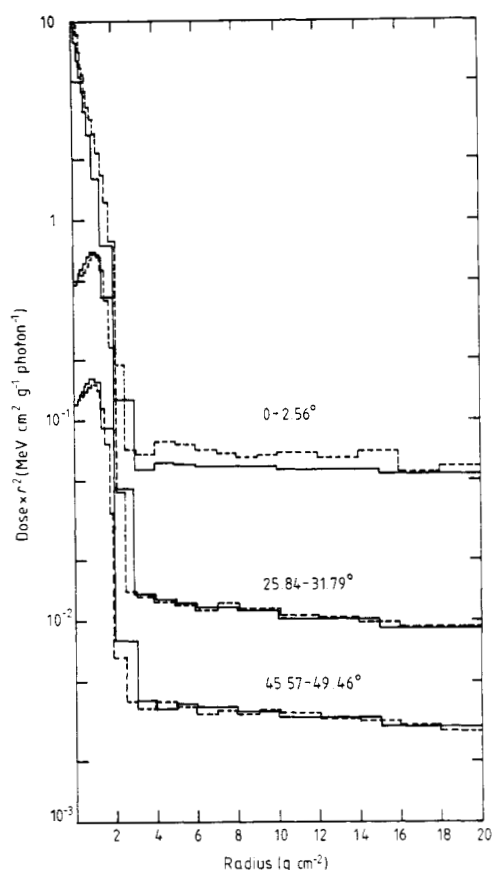


Figure 9. Comparison between the energy deposition kernel for water multiplied by r^2 (—) and differential pencil beams (Chui and Mohan 1986) (---) for 5 MeV incident photons at selected angular intervals.

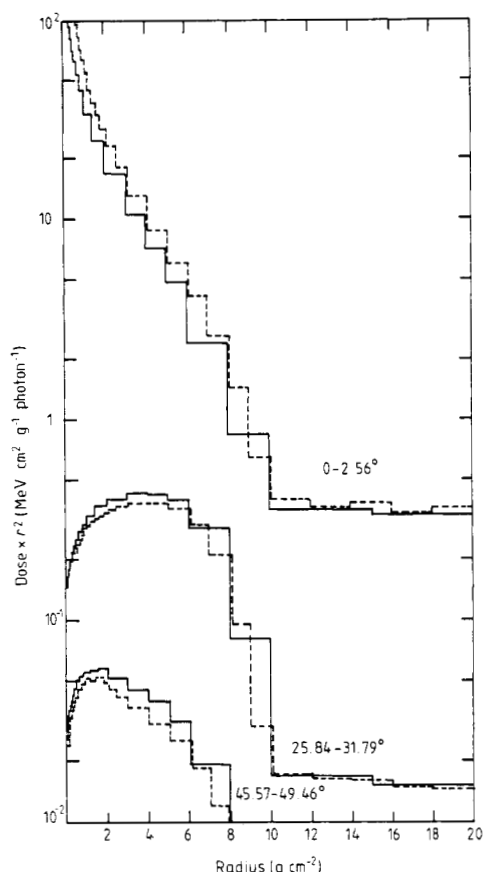


Figure 10. Comparison between the energy deposition kernel for water multiplied by r^2 (—) and differential pencil beams (Chui and Mohan 1986) (---) for 20 MeV incident photons at selected angular intervals.

charged particle range. The total category is the sum of all the components. At small radii, it is dominated by the primary component. The total component would reach an asymptotic value of 1.0 at an infinite radius. These curves can be used to estimate the relative contribution of each component.

4. Applications of the energy deposition kernels

The energy deposition kernels can be used as the kernel in convolution calculations to produce accurate dose distributions for photon beams. The present set has been produced to be of use in a variety of such algorithms. The kernels can be used directly (Mohan *et al* 1986) or they can be transformed into a cylindrical or a Cartesian geometry (Mackie *et al* 1985b). The spectrum of a photon beam can be modelled by repeating a convolution calculation for each spectral component (Chui *et al* 1984). Alternatively, if variations in the incident spectrum are not significant, a kernel can be composed for the spectrum by weighting the kernel at each energy by its contribution to the spectrum (Mackie *et al* 1985b).

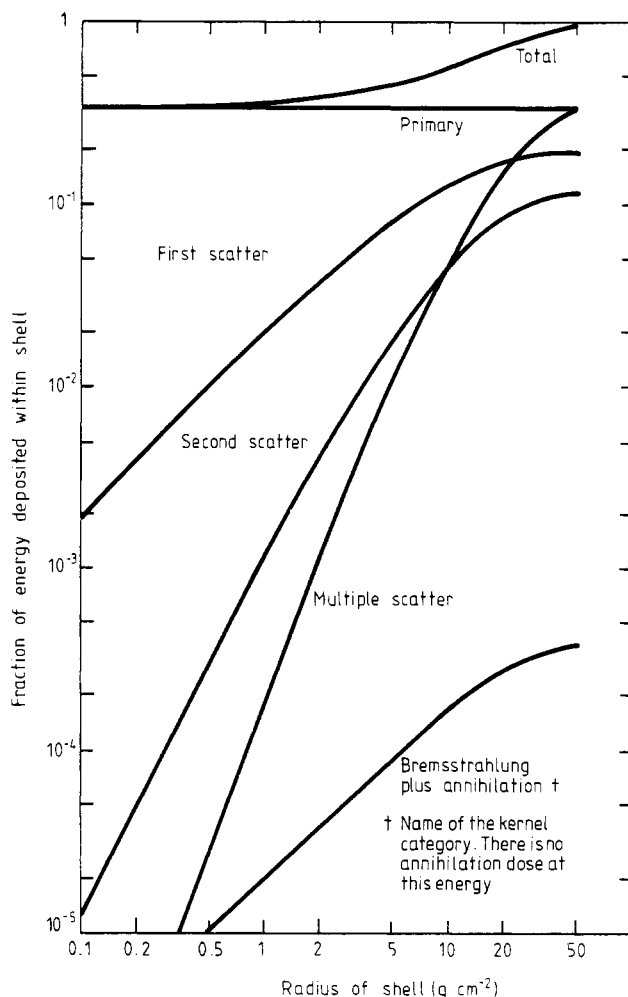


Figure 11. The fraction of incident energy deposited within radial shells as a function of radius for 500 keV photons interacting at the centre of a 60 g cm^{-2} sphere.

A convolution calculation may be done separately for different scattering components of dose. This allows correction for tissue heterogeneity which affects the different scattering components in differing ways (Mackie *et al* 1985b). On the other hand, if the same heterogeneity correction is being employed for all scattering orders the total energy deposition kernel can be used (Mohan *et al* 1986).

The primary energy deposition kernel is difficult to obtain analytically. It can be used in convolution calculations that obtain the scatter convolution kernels analytically (Boyer 1984). In addition, it can also be used to generate the effect of charged particles set in motion from any order of scattering. The photon fluence distribution for the scattering order would be first determined analytically for each scattered photon energy and angle. At each of these energies and angles the primary kernel corresponding to the scattered photon energy would then be weighted with respect to the scattered photon fluence and oriented in the same direction as the scattered photon.

The primary energy deposition kernels can also be used to estimate the transport of charged particles in photon Monte Carlo codes instead of assuming that the energy

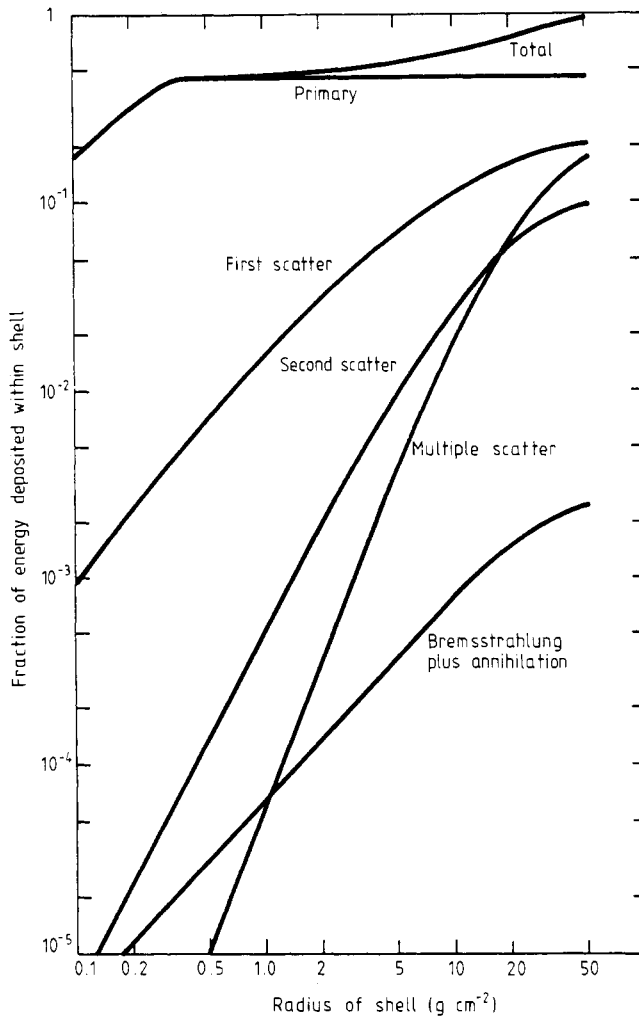


Figure 12. The fraction of incident energy deposited within radial shells as a function of radius for 1.25 MeV photons interacting at the centre of a 60 g cm^{-2} sphere.

is deposited 'on the spot'. Such a hybrid code would not be as accurate as a complete coupled charged-particle-photon Monte Carlo simulation in heterogeneous media and it could not be used to model an electron beam. However, it would have some advantages. It would be more accurate than a Monte Carlo code which models photon transport only. It would be much shorter and easier to write than a traditional Monte Carlo code. Most importantly, it would avoid the calculation time spent in simulating the charged particle path step by step.

5. Conclusions

The energy deposition kernels for all categories were forward peaked at the highest incident photon energies and more isotropically distributed at lower energies. This is compatible with the finding that the amount of energy backscattered from all categories decreases as a function of incident photon energy. The relative amount of energy

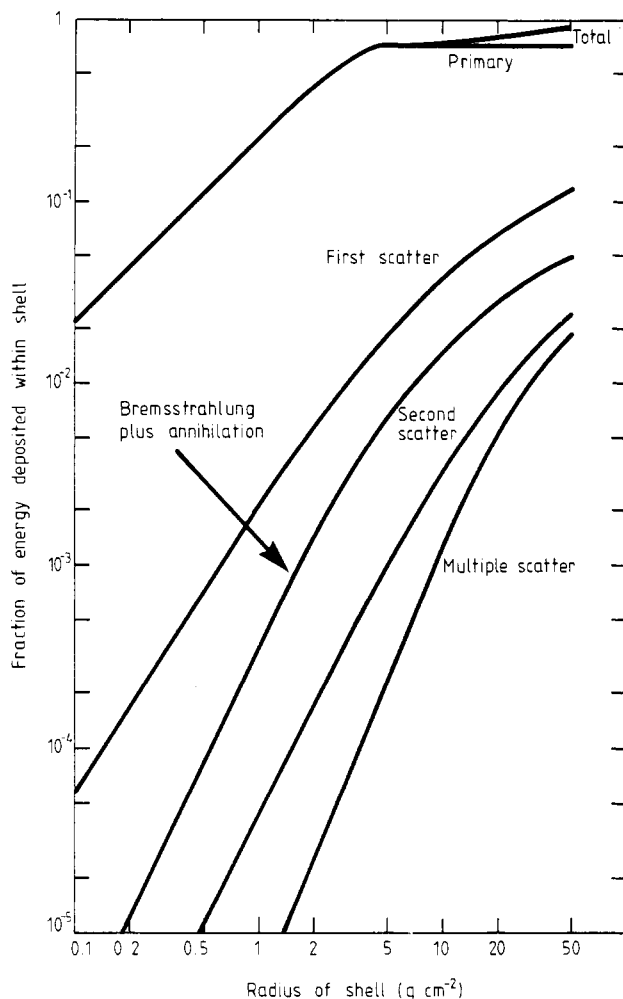


Figure 13. The fraction of incident energy deposited within radial shells as a function of radius for 10 MeV photons interacting at the centre of a 60 g cm^{-2} sphere.

backscattered from the primary component is very small at all incident photon energies. Qualitatively, this indicates that the kernels behave as expected.

Quantitatively, the energy deposition kernels are in good agreement with recent differential pencil beams of Chui and Mohan (1986). Except at the highest photon energies, there is good agreement between the ratio of the total primary energy to the total incident photon energy and the ratio of the energy absorption to the attenuation coefficients. It is likely that our determination of this ratio is superior at high energies because of the inclusion in EGS of positron annihilation in flight.

The mean radii and polar angles weighted with respect to the primary energy deposited in a voxel were calculated for all voxels in which there was primary energy deposited. Together these defined the effective centre of the voxels with respect to the primary component. Except at voxels near the end of the range of the charged particles set in motion, the effective centre of the voxel corresponds to the geometrical centre of the voxel. This indicates that the geometrical centre of the voxel may be used to define the location of the voxel in interpolation routines.

The effective depth of penetration of charged particles \bar{z} for the range of energies investigated was determined using the effective centre of the voxels. This is the first time that a comprehensive determination of \bar{z} has been made for water. A comprehensive determination of the ratio of primary dose to collision kerma for monoenergetic, parallel primary photons interacting in a water phantom, β' , was also done. In addition, simple calculations of β' using the effective penetration depth \bar{z} gave good agreement with the more detailed calculation of β' .

The energy deposition kernels and Fortran-77 routines to read them are available on computer tape from the authors.

Acknowledgments

The authors would like to thank Robert Andrews at the Allan Blair Memorial Clinic, Regina and Colin Field at the Cross Cancer Institute, Edmonton for their programming assistance and to acknowledge the lively discussions with Peter Dickof at the Allan Blair Memorial Clinic, Arthur Boyer at the MD Anderson Hospital, Houston, Anders Ahnesjö, University of Uppsala, Uppsala, Sweden and Chen Chui and Radhe Mohan at Memorial Sloan Kettering Cancer Institute, New York. The financial support of the Saskatchewan Cancer Foundation is gratefully accepted. The excellent art work of Dave Weir at the University of Regina is greatly appreciated.

Résumé

Génération de grains de dépôt d'énergie de photons en utilisant des codes EGS simulés par la méthode de Monté Carlo.

Les auteurs utilisent des codes EGS simulés par la méthode de Monté Carlo afin de générer des grains de perte d'énergie des photons, qui décrivent l'énergie déposée par les particules chargées mises en mouvement par des photons de première diffusion, de seconde diffusion, multi-diffusés, des photons de freinage ainsi que des photons d'annihilation. Ils sont calculés pour de l'eau irradiée au moyen de photons monoénergétiques dans le domaine 0,1 à 50 MeV. En plus des grains de dépôt d'énergie des particules primaires, le transport des particules primaires chargées a été caractérisé en calculant le centre effectif des voxels, ainsi que la profondeur de pénétration effective, le rayon effectif et la distance effective latérale parcourue par ces particules. Les auteurs ont calculé la dose β' par unité de kerma par collision pour un faisceau parallèle de photons primaires monoénergétiques. Ils ont discuté d'autres applications des grains de dépôt d'énergie.

Zusammenfassung

Die Simulation der Energieübertragung von Photonen mit Hilfe des EGS-Monte Carlo-Programmes.

Zur Simulation der Energieübertragung von Photonen, die durch geladene Teilchen, ausgelöst durch Primärphotonen, Photonen durch Einfachstreuung, Zweifachstreuung, Mehrfachstreuung und Bremsstrahlung plus Vernichtungsstrahlung erfolgt, wurde das EGS-Monte Carlo-Programm verwendet. Die Berechnungen wurden durchgeführt für Bestrahlung von Wasser mit monoenergetischen Photonen mit Energien zwischen 0,1–50 MeV. Zusätzlich zur primären Energieübertragung wurde der Transport geladener Primärteilchen weiter beschrieben durch die Berechnung der effektiven Voxelmittelpunkte, sowie durch Berechnung der effektiven Eindringtiefe, des effektiven Radius und der effektiven lateralen Entfernung, die von diesen Teilchen zurückgelegt wird. Die Dosis pro Collision-kerma-Einheit für parallel einfallende monoenergetische Primärphotonen, β' , wurde berechnet. Zusätzliche Anwendungen der Energieübertragungsberechnungen werden diskutiert.

References

- AAPM 1983 *Med. Phys.* **10** 741–71
 Ahnesjö A 1984 *Proc. 8th Int. Conf. on Computers in Radiotherapy (Toronto)* pp 17–20

- Bielajew A F, Rogers D W O and Nahum A E 1985 *Phys. Med. Biol.* **30** 419-27
- Boyer A L 1984 *Med. Phys.* **11** 552-4
- Boyer A L and Mok E C 1984 *Proc. 8th Int. Conf. on Computers in Radiotherapy (Toronto)* pp 14-16
- 1985 *Med. Phys.* **12** 169-77
- Brahme A 1977 *Report SSI:1977-009* National Institute of Radiation Protection, Stockholm
- Chui C and Mohan R 1986 private communication
- Chui C, Mohan R and Lidofsky L 1984 *Med. Phys.* **11** 392 (abstract)
- Dean R D 1980 *Med. Phys.* **7** 429 (abstract)
- Ford R L and Nelson W R 1978 *The EGS Code System, Stanford Linear Accelerator Report 210* (Stanford, CA: Stanford Linear Accelerator)
- Hubbell J H 1969 *Photon Cross Sections, Attenuation Coefficients, and Energy Absorption Coefficients from 10 keV to 100 GeV* NSRDS-NBS No 29 (Washington, DC: US Govt Printing Office)
- 1977 *Radiat. Res.* **70** 58-81
- 1982 *Int. J. Appl. Radiat. Isot.* **133** 1269-90
- Johns H E and Cunningham J R 1983 *The Physics of Radiology* 4th edn (Springfield, IL: Thomas)
- Loevinger R 1981 *Med. Phys.* **8** 1-12
- Mackie T R 1983 *Med. Phys.* **10** 536 (abstract)
- 1984 *PhD thesis* University of Alberta
- Mackie T R, El-Khatib E, Scrimger J W, Battista J J, Van Dyk J and Cunningham J R 1985a *Med. Phys.* **12** 327-32
- Mackie T R and Scrimger J W 1984 *Proc. 8th Int. Conf. on Computers in Radiotherapy (Toronto)* pp 36-40
- Mackie T R, Scrimger J W and Battista J J 1985b *Med. Phys.* **12** 188-96
- McEwan A C and Smyth V G 1984 *Med. Phys.* **11** 216-8
- Mohan R and Chui C 1985 *Med. Phys.* **12** 726-30
- Mohan R, Chui C and Lidofsky L 1985 *Med. Phys.* **12** 592-7
- 1986 *Med. Phys.* **13** 64-73
- NACP 1980 *Acta Radiol. Oncol.* **19** 55-79
- 1981 *Acta Radiol. Oncol.* **20** 401-15
- Nelson W R, Hirayama A and Rogers D W O 1985 *The EGS4 Code System, Stanford Linear Accelerator Report 265* (Stanford, CA: Stanford Linear Accelerator)
- Roesch W C 1958 *Radiat. Res.* **9** 399-410
- Rogers D W O 1982 *Nucl. Instrum. Meth. Phys. Res.* **199** 531-48
- 1984 *Nucl. Instrum. Meth. Phys. Res.* **227** 535-48
- Rogers D W O and Bielajew A F 1985 *Med. Phys.* **12** 738-44
- Schulz R J and Loevinger R 1984 *Med. Phys.* **11** 218